HHS Public Access

Author manuscript

Brain Stimul. Author manuscript; available in PMC 2022 March 03.

Published in final edited form as:

Brain Stimul. 2021 ; 14(5): 1205–1215. doi:10.1016/j.brs.2021.08.003.

Individualized tDCS Modeling Predicts Functional Connectivity Changes within the Working Memory Network in Older Adults

Aprinda Indahlastari, Ph.D.[1,2,†], **Alejandro Albizu, B.S.**[1,3], **Jessica N. Kraft, M.A.**[1,3], **Andrew O'Shea, M.Sc.**[1,2], **Nicole R Nissim, Ph.D.**[1,3], **Ayden L Dunn**[1], **Daniela Carballo**[1,2], **Michael P Gordon**[1,2], **Shreya Taank**[1], **Alex T Kahn**[1], **Cindy Hernandez**[1,2], **William M Zucker**[1], **Adam J. Woods, Ph.D.**[1,2,3]

[1]Center for Cognitive Aging and Memory, McKnight Brain Institute, University of Florida, Gainesville, FL

[2]Department of Clinical and Health Psychology, University of Florida, Gainesville, FL

[3]Department of Neuroscience, University of Florida, Gainesville, FL

Abstract

Background: Working memory decline has been associated with normal aging. The frontal brain structure responsible for this decline is primarily located in the prefrontal cortex (PFC). Our previous neuroimaging study demonstrated a significant change in functional connectivity between the left dorsolateral PFC (DLPFC) and left ventrolateral PFC (VLPFC) when applying 2mA tDCS in MRI scanner during an N-back task. These regions were part of the working memory network. The present study is the first study that utilizes individualized finite element models derived from older adults' MRI to predict significant changes of functional connectivity observed from an acute tDCS application.

Methods: Individualized head models from 15 healthy older adults (mean age=71.3 years) were constructed to create current density maps. Each head model was segmented into 11 tissue types: white matter, gray matter, CSF, muscle, blood vessels, fat, eyes, air, skin, cancellous, and cortical bone. Electrodes were segmented from T1-weighted images and added to the models. Computed median and maximum current density values in the left DLPFC and left VLPFC regions of interest (ROIs) were correlated with beta values as functional connectivity metrics measured in different timepoint (baseline, during stimulation) and stimulation condition (active and sham).

Main results: Positive significant correlations (R^2=0.523 for max J, R^2=0.367 for median J, $p<0.005$) were found between the beta values and computed current densities in the left DLPFC ROIs for active stimulation, but no significant correlation was found during sham stimulation. We found no significant correlation between connectivity and current densities computed in the left VLPFC for both active and sham stimulation.

Conclusions: The amount of current within the left DLPFC ROIs was found positively correlated with changes in functional connectivity between left DLPFC and left VLPFC during

[†]**Please address correspondence to**: Aprinda Indahlastari, Ph.D., Department of Clinical and Health Psychology, University of Florida, Gainesville, FL, USA, Phone: (352) 294-8631, aprinda.indahlas@phhp.ufl.edu.

Disclosure: The authors report no conflicts of interest.

active 2mA stimulation. Future work may include expansion of number of participants to further test the accuracy of tDCS models used to predict tDCS-induced functional connectivity changes within the working memory network.

Keywords

tES; tDCS; aging; working memory; finite element model

INTRODUCTION

Anatomical and functional changes in the brain can occur with normal aging and have been associated with decline in brain function [1–4]. In particular, the prefrontal cortex (PFC) exhibits strong age-related changes that affect cognition (e.g., working memory) [1]. The working memory process is critical for decision-making and activities of daily living and thus age-related cognitive decline can cause loss of independence that could impact the quality of life [5,6]. Prior research has explored neuroimaging measures such as structural and functional magnetic resonance imaging (fMRI) to investigate the neural correlates of working memory performance in older adults [7–9]. For instance, Cabeza et al. reported that high-performing older adults exhibited bilateral recruitment of frontal structure (neural compensation hypothesis) compared to low performing older adults who exhibited a significant increase of the right lateralized blood-oxygenation-level-dependent (BOLD) response during a working memory task [8]. Therefore, effective intervention strategies are needed to further explore potential means to improve working memory performance affected by normal aging.

Transcranial direct current stimulation (tDCS) is a form of non-invasive brain stimulation and has the potential to impact cognitive processes, such as remediating age-related cognitive decline in older adults [10]. In conventional tDCS, a pair of large electrodes (e.g., ~35cm^2) are fixed on the scalp to deliver a constant current at ~1–2mA [11,12]. One domain of cognitive processes that can benefit from tDCS application is working memory [13–15]. Prior research shows that tDCS application during a working memory task can increase training gains and suggests the efficacy of pairing tDCS with working memory task is state dependent [16,17]. A prior neuroimaging study from our research group [18] investigated the acute effects of an in-scanner 2mA tDCS application over the frontal cortex of healthy older adults during working memory tasks. The prior study found a significant increase in functional connectivity between the left dorsolateral prefrontal cortex (lh-DLPFC) and left ventrolateral prefrontal cortex (lh-VLPFC) during active stimulation, but not during sham stimulation.

In-vivo measurements of tDCS electrical current distribution in the brain are difficult to accomplish and thus MRI-derived computational modeling has been used to estimate delivered tDCS current dose in the brain [19–21]. These computational models use finite element method (FEM) to construct realistic head models derived from structural MRI data such as T1- and T2-weighted images. Constructing individualized models that are unique to each person improves estimates of tDCS current distribution in the brain because these models account for inter-individual anatomical differences [22–24]. Prior research shows

that estimated field measures generated from tDCS computational models can be used to predict associated tDCS-induced changes seen in acquired functional MRI (fMRI) data. For instance, Halko et al. [25] compared field measures generated from tDCS models to fMRI BOLD activation in a 61-year-old stroke patient, and found a positive correlation ($r=0.308$, $p<0.05$) between calculated maximum electric field within the occipital cortex and changes in fMRI BOLD response in the occipital lobe. Jamil et al. [26] performed a correlation analysis in 29 young adults (mean age(SD): 25(4.4) years) to investigate the relationship between tDCS-induced cerebral blood flow measured via arterial spin labeling and electric fields generated from a single FEM model derived from an MNI template head. They reported a similar relationship where the maximum electric field within the primary motor cortex was positively correlated ($r=0.204$, $p<0.0001$) with measured cerebral blood flow. Antonenko et al. [27] was the first study to use FEM to investigate functional connectivity changes induced by tDCS. They performed FEM modeling study in 24 tDCS recipients (mean age (SD): 25(4) years) and found a positive correlation between the normal component of computed electric fields and the sensorimotor network strengths derived from functional connectivity measurements of resting-state fMRI within the precentral gyrus. However, there has not been a tDCS computational study that investigates the relationship between estimated current dose in the brain and measured functional connectivity changes within the working memory network resulting from tDCS application in an older adult population.

In a recently published paper from our research group [18], Nissim et al. reported a mechanistic study investigating the acute effects of a single session in-scanner bilateral tDCS (2mA, 12 minutes) on functional connectivity of the working memory network in healthy older adults. The prior study found significant connectivity changes between lh-DLPFC and lh-VLPFC during an active tDCS stimulation paired with an N-back task [18]. Specifically, the connectivity changes were measured as beta values within spherical regions of interest (ROIs) that were located within lh-DLPFC and lh-VLPFC. The spherical ROIs were derived from a meta-analysis conducted by Owen et al. [9] that reported MNI coordinates for the nodes that are representative of the working memory network. In the present study, we generated current density maps using individualized FEM modeling derived from the same participants to predict previously reported tDCS-induced functional connectivity changes within the working memory network [18]. The present study is the first modeling study performed on the acute in-scanner tDCS dataset reported in Nissim et al. [18]. Since the prior study performed an in-scanner tDCS, the electrode pads and paste were captured as part of the structural MR data (T1-weighted images). Therefore, the electrodes were manually segmented directly from the T1-weighted images. In the present study, we hypothesized that computed current density within the same ROIs would be positively correlated with the beta values measured during active stimulation, but not with the beta values measured during sham stimulation. Further, computed current densities within each ROI may provide insight into the relationship between the role of current dose delivered in each ROI and the observed significant changes in functional connectivity between these two ROIs.

METHODS

Detailed information regarding participant recruitment, screening, inclusion/exclusion criteria, and study methods can be found in the previously published study [18]. In brief, sixteen older adults (age range=61–82 years, mean age=71.8 years, 6 females, mean education=16.8 years) that were deemed as healthy older adults defined as cognitively intact/cognitively healthy individuals, without any form of neurodegenerative diseases and cognitive impairment. The screening process to confirm cognitively healthy in each participant was based on a Montreal Cognitive Assessment (MoCA) score of 20 and above. Each participant underwent an in-scanner tDCS and had two MRI sessions paired with one active and one sham tDCS. One participant was excluded from the present modeling study due to poor SNR in the acquired T1-weighted data. The remaining fifteen T1-weighted images were converted into head models for generating field maps. Computed current density values were compared to significant beta values that were calculated in previously performed functional connectivity analyses [18]. Additional details on neuroimaging methods, stimulation information, and modeling workflow are described in the following subsections.

Functional MRI and tDCS Application

Imaging Acquisition—Individual T1-weighted images were acquired using MPRAGE sequence in 3T Phillips Achieva MRI scanner (FOV=240×240×170mm, voxel size=1mm^3, TR=7ms, TE=3.2ms, flip angle=8°) prior to fMRI data acquisition. fMRI images were acquired using a single-shot EPI sequence (36 slices, voxel size 3.5mm^3, TR=2000ms, TE=30ms, flip angle=80°). All scans were collected using a 32-channel head coil.

tDCS Parameter and fMRI Paradigm—During fMRI data acquisition, participants performed a series of N-back tasks aimed at activation of the working memory network while under both sham and active stimulation. A total of three N-Back task with 12 minutes duration each was performed in-scanner by participants before (baseline), during and after stimulation. Details on the N-Back task can be found in the prior study [18]. Conventional tDCS with 5×7cm^2 rubber pad electrodes in F3 (cathode) and F4 (anode) location was applied inside the MRI scanner (in-scanner tDCS) during the fMRI paradigm. Each participant received one dose of active stimulation and one dose of sham during a separate MRI visit. Stimulation of 2mA was applied using the neuroConn DC-Stimulator MR for 12 minutes during active condition and 30 seconds during sham condition with 30 seconds ramp up/down. Stimulation duration of 12 minutes total was selected to match the duration of the N-Back task length. A layer of approximately 5mm thick electric conductive paste (Ten20 paste) was applied at the interface between the rubber pad electrode and the scalp, and the electrodes were held in place using a rubber Soterix Easy-Head strap. The stimulation delivery was double-blinded and the order of active and sham tDCS was counterbalanced across participants.

Functional Connectivity Analysis—Two spherical regions of interest (ROIs) created using the Wake Forest University (WFU) PickAtlas [28,29] and the MNI-coordinates from Owen et al. [9] were selected based on seed-to-target ROIs in our published functional

connectivity analysis study [18]. The two ROIs consisted of a ~129mm^3 sphere within lh-DLPFC and a ~314mm^3 sphere within lh-VLPFC [18]. Functional connectivity analysis was performed using CONN Toolbox v.2017.f[1] to compute beta values between the two ROIs during active and sham stimulation. In CONN, model contrasts comprised various timepoint (baseline, during stimulation) and stimulation condition (active, sham) were defined within a single stimulation session. A significant increase in functional connectivity seeding between lh-DLPFC ROI and lh-VLPFC ROI for during-active over baseline-active contrast (during-active>baseline-active) was found. The CONN denoising pipeline identifies potential noise areas from BOLD images, particularly within two anatomically defined regions namely white matter and CSF. During this step, regions within white matter and CSF probability masks with intensity above 50% were applied a one-voxel binary erosion.

Computational Modeling

Model Construction—All acquired fifteen T1-weighted images were segmented into eleven tissue types using a combination of manual and automatic segmentation process following a pipeline described in Appendix A. Each tissue type was assigned unique conductivity values derived from the literature [20,30–33]. White matter, gray matter, CSF, and skin were assigned conductivity values of 0.126S/m, 0.276S/m, 1.65S/m, and 0.465S/m, respectively [30,34]. Muscle, fat, blood vessels, and eyes conductivity values were assigned as 0.16S/m, 0.25S/m, 0.67S/m, and 0.5S/m, respectively [20]. Conductivity values of 21.4e^{-3}S/m and 5.52e^{-3}S/m were assigned to cancellous and cortical bone, respectively [33]. Automatic segmentation process for bone, skin and air was completed using SPM 12 [35] and corrected manually in Simpleware ScanIP module (Synopsys, Exeter, UK). All manual segmentation work for the remaining tissue masks was performed in Simpleware ScanIP with a reference to an atlas. White and gray matter masks that were previously used in CONN analysis were imported to Simpleware and combined with the rest of segmented tissue volumes. Since the electrodes were visible in T1-weighted images, the rubber pad electrodes and paste were manually segmented directly from T1-Weighted images and assigned conductivity values of 1S/m [19] and 0.3178S/m [36], respectively.

Volume Meshing and Model Solution—Segmented head volumes were converted into volume meshes in Simpleware ScanFE module and meshed models were exported to COMSOL 5.2a for finite element formulation and solution. Terminal current boundary conditions of 2mA at F4 and −2mA at F3 were assigned to the model using COMSOL AC/DC module [19]. The models were then solved for voltage and converted to current density values using COMSOL-MATLAB Livelink Interface.

Current Density Analysis—Generated current density maps in each model were restricted using a custom mask containing gray matter, white matter, and CSF compartment. A one-voxel binary erosion of white matter and CSF was performed following the CONN denoising pipeline outlined in Functional Connectivity Analysis section and combined with the custom mask. After the masking process, each current density volume was linearly transformed into the WFU PickAtlas space using FSL FMRIB's Linear Registration Tool (FLIRT) [37] and applied the full-width at half maximum (FWHM) Gaussian smoothing kernel in SPM with the same setting (8×8×8mm kernel size) as BOLD image processing.

Median and maximum values of smoothed current densities were computed in each ROI and compared to the beta values obtained from prior connectivity analysis [18] for active and sham stimulation in each participant. The median values were used to represent central tendency of current density distribution within ROIs. The mean values were omitted to avoid skewed values affected by partial volume effects (e.g., outliers from large spikes at tissue boundary between CSF and gray matter regions) [19,20]. The maximum current density was selected following prior research in this topic [25] and computed as a single peak value within each ROI in each head model. Only beta values measured for contrast stimulation over baseline (during>baseline) were compared to current density values. Beta values measured during the sham stimulation were included in the analysis to investigate the specificity between estimated current density values and types of stimulation (active or sham). A correlation analysis was performed between computed current densities and beta values using SPSS package Version 25 [38] and converted to Cohen's d [39]. In addition, regression analyses were performed to test the effect of age, weight, height, and head fat content on computed electric fields. Head fat content was computed by counting the number of voxels of fat compartment in each head and normalize them according to voxel count of soft tissues in each head (fat, muscle, and skin) [40].

RESULTS

Electric field and current density maps were generated from fifteen segmented head volumes and further quantified within the two spherical ROIs: lh-DLPFC and lh-VLPFC. The maximum and median values of computed current densities in each ROI were correlated to the beta values measured during active but not sham stimulation. Demographic factors such as age, weight, height, and body mass index (BMI) of each participant are reported in Appendix B. None of the demographic factors or head fat content were found significantly correlated to computed field measures as shown in Appendix C. Details of model quality and current density analyses are reported in the following subsections.

Segmentation quality and electrode placement

Figure 1 illustrates an overlay of a T1-weighted image and the segmented head volume in a single head model consists of eleven tissue types and two sets of electrode's paste and pad. Each of the eleven tissue types and the additional segmented electrodes underwent a series of quality assessments to ensure there was no gap between adjacent tissue types and that individual tissues were within their respective tissue boundaries in all image slices. Figure 2 shows the individual location of manually segmented electrodes (combination of pad and paste) in fifteen participants with red denoting the anode and blue denoting the cathode location. While the study aimed to stimulate using F4 (red) as anode and F3 (blue) as cathode location, there was a slight variation of electrode location across participants for both the anodes and the cathodes as illustrated in Figure 2.

Overall current density distribution

Computed field maps in each head model are shown in Figure 3. Overall, field patterns across individuals were varied and non-identical. As expected, the overall pattern of field measures showed larger values concentrated towards the frontal regions near the

electrodes and smaller values distributed towards the posterior of the brain, further away from the electrodes. Generated current density maps after being processed with custom masks according to the denoising pipeline in CONN are shown as axial slices in Figure 4. Application of the Gaussian filter to generated current densities produced smoothed or blurred texture of distributed current density values, comparable to the appearance of processed BOLD images as seen in Figure 4. The black and red circles overlaid onto the BOLD images illustrated the location of the spherical ROIs in the lh-DLPFC and the lh-VLPFC, respectively.

Current density in the left DLPFC ROI

The overall average of median current density (J[A/m^2]) across fifteen participants within lh-DLPFC ROI was 0.0814Am^{-2}. The maximum current density computed in lh-DLPFC ROIs for all fifteen participants was 0.1094Am^{-2}. Figure 5 shows the correlation plots between computed current densities in lh-DLPFC ROIs and measured beta values during active and sham stimulation. The correlation plot in Figure 5A shows a significant positive relationship between the beta values measured during active stimulation and the maximum current density values in lh-DLPFC ROIs (R^2=0.523, p=0.0023). Computed median current densities within lh-DLPFC are also significantly correlated with the beta values measured during active stimulation (R^2=0.367, p=0.0168) as shown in Figure 5B. There was no correlation between computed maximum and median current density values within lh-DLPFC ROIs and measured beta values for the sham stimulation (Figure 5C, 5D).

Current density in the left VLPFC ROI

The average median current density within lh-VLPFC ROIs computed in fifteen participants was 0.0529Am^{-2}, while the maximum current density was 0.0829Am^{-2}. The correlation plots between computed current densities and measured beta values are reported in Figure 6. We found no correlation between computed maximum and median current densities in lh-VLPFC ROIs and the beta values measured during active stimulation (Figure 6A–B). There was also no correlation between computed current densities and measured beta values for sham stimulation as illustrated in Figure 6C and 6D.

DISCUSSION

The primary goal of the present study is to evaluate the relationship between the current dose within brain regions during an acute application of tDCS and resulting significant functional connectivity changes. We performed detailed FEM modeling in each individual by carefully segmenting each T1-weighted image into eleven tissue types in fifteen healthy older adults receiving an in-scanner tDCS during a working memory task. Unique to most tDCS computational modeling studies, the electrode pad and paste were visible in individual T1 images and thus were manually segmented and combined with the rest of segmented tissue volumes. Current density maps from each participant were then post-processed following the same pipeline as the BOLD image processing that was used to perform functional connectivity analysis. Computed current densities in post-processed models and measured significant beta values were compared in each ROI. We found a significant positive correlation ($p<0.05$) between measured beta values during active stimulation and

computed current densities within lh-DLPFC ROIs. The findings from this study will be discussed further in the following subsections.

Model Validity

Manual tissue segmentation performed in each person allowed additional tissue characteristics incorporated into the models, creating a more realistic tissue representation in older adults, and, in turn, an improved current density estimation. Each of the eleven tissue types were non-identical and shaped differently across participants. Individual shapes of tissue regions were assigned unique conductivity values, and thus dictate the patterns of electrical current distribution in each person as shown in Figure 3–4. For example, the adipose tissue or fat composition in each head model was varied across participants, and the inclusion of fat compartment has been found to affect current density prediction by up to 60 [40]. We found non-significant relationship between electric field and head fat content (R^2=0.202, p=0.092), as shown in Appendix C. The non-significance effect of fat on computed field measure might be caused by the inclusion of a large number of tissue types (eleven tissue types) within our head models. This finding aligned with observation reported by Truong et al., stating that the relative contribution from head fat tissue on current density was found small when other components of head anatomy were added [40]. In addition, accurate representation of bone tissue is important in the generated electric field due to its resistive property [41]. Further separation of the skull compartment into cancellous and cortical bone is crucial in older adults since bone degradation or osteoporosis causing the bone to be more porous (i.e., more spongy or cancellous) is more likely to occur with older age especially in female [42]. A considerable portion of cancellous versus cortical bone can be seen in the T1 image (Figure 1A) where the cancellous portion appears brighter than cortical tissue within skull compartment as well as in segmented volume (Figure 1C). Spongy or cancellous bone is comprised of bone marrow that is more conductive compared to compact or cortical bone. Therefore, the individual differences of cancellous and cortical bone composition across participants contributed to more realistic representation of tissue organization in older adults and thus reflected in generated current density estimates in each person, which support prior studies in this domain of the importance in including cortical and cancellous bone [41,43,44].

Electrodes segmented from individual T1 images captured actual electrode location that depict a more accurate prediction of delivered current density distribution in individual brain regions. Since this modeling study was performed on an in-scanner tDCS, the precise electrode location was captured during imaging and thus the electrodes were visible in the T1-weighted scans. The exact electrode location was crucial to formulate more accurate boundary conditions in the model where electrical current was applied and removed (anode and cathode location). In addition to capturing accurate location of the electrodes, the segmented electrodes also provided a more accurate representation of contact areas since the input current density is quantified base on the total amount of current divided by the contact area. Thus, the location of modeled contact areas in this study are true representation of actual electrode placements. While available current flow modeling toolboxes include electrode placement routine, the electrodes are artificially placed in their ideal location based on the 10–20 EEG system that may not be an exact replica of actual electrode location used

during tDCS session. Further, any shifts within electrode location as little as 1cm have been shown to have a profound effect on delivered current dose in the brain [11,44,45]. Therefore, our models are considered more accurate by incorporating actual electrode placement, in terms of location, orientation, and contact area instead of adding artificially made electrodes that are placed in their ideal locations based on the 10–20 EEG system prior to calculating current density distribution.

Model Implications

Our modeling results further support the importance of incorporating each person's anatomical characteristics to estimate tDCS current delivery at an individual level shown by the relationship seen between computed field measures and changes in functional connectivity. The levels of current dose delivered to each brain across fifteen participants were varied, indicated by a range of computed median and maximum current densities in each ROI despite employing the same tDCS parameters (electrode location, input current, etc.). This finding demonstrates that the difference in anatomy across different individuals contributed to various levels of current dose found in the brain. Further, individual current density values corresponded to individual changes in functional connectivity between brain regions, underlining the importance of individualized modeling. For instance, the anatomical details included in our models, such as the amount of cortical bone or CSF, may affect current pattern in the brain. Therefore, modeled tissue shape and organization that were unique to each person might be crucial to observed connectivity changes in each individual. If the models were generated by using a single template head model, no variation would have been seen in their computed current densities and thus would omit the distinct relationship seen between various current dosage in each participant and their respective measured beta values. Additionally, studies within the tDCS field often result in mixed findings [15]. This may be due, in part, by not taking into account individual head anatomical differences which cause varying amounts of current to reach the underlying tissues. Using the head modeling approach in the current paper will allow for greater accuracy and replicability with the tDCS field. Therefore, the construction of individualized head models proves to be a robust and promising tool to predict individual changes in measured functional connectivity induced by tDCS.

Our findings suggested that the current dose contained within lh-DLPFC contributed to the significant changes in functional connectivity within the working memory network induced by active tDCS. Out of several combinations of spherical ROIs placed within the working memory network, the prior study found significant changes in functional connectivity between lh-VLPFC and lh-DLPFC ROIs during active stimulation. Prior research has shown that the VLPFC has exhibited increased activity for various cognitive control processes while the DLPFC has shown an important contribution towards maintaining, manipulating and retrieving information during task delay periods [46–50]. Increased connectivity between these two regions suggests enhanced activity in cognitive control processes, which is relevant to the working memory domain. Computing the current dose in each of these regions provides insight into which of the two brain regions played a larger role in observed significant changes of functional connectivity between the two ROIs. Prior studies have shown promising results of enhanced activity in the DLPFC regions resulting from brain

stimulation [51,52]. Applying tDCS with F3-F4 electrode placement is typically chosen to aim current delivery to the DLPFC region [15], which is approximately directly underneath and between the electrode pair. As expected, current delivered within the DLPFC region was found to be larger in magnitude compared to the VLPFC due to the proximity of electrode placement. Further, we found a significant positive correlation with large effect size (Cohen's d=2.094, R^2=0.523 for max J, R^2=0.367 for median J, $p<0.005$) between computed current densities in lh-DLPFC ROIs and measured connectivity during active stimulation. No significant correlation was found between computed current densities in lh-VLPFC and measured connectivity. Therefore, our findings implied that significant changes in functional connectivity between lh-DLPFC and lh-VLPFC during a pairing between a working memory task and acute tDCS application were driven by the amount of current delivered to the left DLPFC area. These findings suggest that future dosing strategies should consider maximizing current delivery at targeted brain region to optimize stimulation outcomes associated with that region. Taken together, our study suggests the potential benefit of pairing computational modeling and neuroimaging methods by isolating current characteristics and corresponding functional changes that may allow future formulation of precision dosing applications to maximize tDCS effects.

The lack of significant correlation between current density and functional connectivity during sham stimulation indicates specificity of the relationship between estimated current densities and a brief stimulation duration. The sham stimulation only consisted of a brief current application of 30 sonds at the start of the N-Back task with 30s ramp up/down. We found that the estimated current dose in both ROIs did not have a significant correlation with measured connectivity during sham stimulation which suggests that functional connectivity captured during sham stimulation was not affected by the brief presence of electrical current. Therefore, our models demonstrate that estimated current density was able to capture the changes caused by active stimulation and not sham stimulation, indicating evidence of a mutual relationship between current dose delivery and measured connectivity change during active stimulation.

Model limitation and future direction

We acknowledge a number of limitations present in our study. While individual tissues were manually corrected and segmented, the resolution of each tissue type was limited by the resolution of the MR scans ($1mm^3$). There might be a partial volume effect that may cause the head model to be less accurate and, in turn, affecting estimated current density in each ROI. Similarly, estimated field measures are highly dependent on assigned conductivity values in each tissue. We used the most common set of conductivity values performed in prior tDCS computational studies [30,31]. As in-vivo measurements of conductivity values become available, it is crucial to rerun these models and obtain the most accurate estimation possible. In addition, future studies can utilize higher resolution images, if available, to further improve model estimation. We also acknowledge the small number of participants (N=15) included in this study. A larger cohort study is required to further test the validity of model prediction in estimating functional connectivity changes in the working memory network. A similar modeling pipeline can be used by incorporating different tDCS parameters (e.g., electrode location, electrode size, current dose) to predict

functional connectivity in other brain networks, such as the default mode network or sensory-motor network to investigate the relationship between current dose and changes in functional connectivity. Further, additional connectivity analyses using anatomical based ROIs in addition to spherical ROIs might be useful in capturing any functional changes outside spherical ROIs and within anatomically defined brain regions affected by delivered tDCS. Registering individual heads to a more appropriate older adult based template such as the UFAB-587 [23] may also increase the accuracy of analyzing functional data in older adult cohort since structural decline such as brain atrophy would be counted when analyzing relevant brain regions. In addition, performing a multivariate approach on generated models in future study can be beneficial to further explore contributions of median and maximum current densities to observed connectivity due to tDCS.

CONCLUSION

We present the first computational study to evaluate the relationship of current dose and resulting functional connectivity from an acute tDCS application targeting the working memory network in older adults. We found a significant correlation between the amount of current density delivered to the left DLPFC and measured functional connectivity between the left DLPFC and the left VLPFC during tDCS application paired with the N-Back task. Our findings indicate that the large amount of current dose within the left DLPFC may be important for eliciting functional connectivity changes within the left DLPFC and the left VLPFC. Our modeling results provide insight for future studies that focus on dosing strategy [53] to maximize stimulation outcomes within the working memory network.

Supplementary Material

Refer to Web version on PubMed Central for supplementary material.

ACKNOWLEDGEMENTS

This work was supported in part by the National Institute of Aging/National Institutes of Health (K01AG050707, R01AG054077), the Evelyn F. and William L. McKnight Brain Research Foundation, and the University of Florida Center for Cognitive Aging and Memory.

REFERENCES

[1]. Nissim NR, O'Shea AM, Bryant V, Porges EC, Cohen R, Woods AJ. Frontal structural neural correlates of working memory performance in older adults. Front Aging Neurosci 2017;8. doi:10.3389/fnagi.2016.00328.

[2]. Hausman HK, O'Shea A, Kraft JN, Boutzoukas EM, Evangelista ND, Van Etten EJ, et al. The Role of Resting-State Network Functional Connectivity in Cognitive Aging. Front Aging Neurosci 2020;12. doi:10.3389/fnagi.2020.00177.

[3]. Kraft JN, O'Shea A, Albizu A, Evangelista ND, Hausman HK, Boutzoukas E, et al. Structural Neural Correlates of Double Decision Performance in Older Adults. Front Aging Neurosci 2020. doi:10.3389/fnagi.2020.00278.

[4]. Hardcastle C, O'Shea A, Kraft JN, Albizu A, Evangelista ND, Hausman HK, et al. Contributions of Hippocampal Volume to Cognition in Healthy Older Adults. Front Aging Neurosci 2020;12. doi:10.3389/fnagi.2020.593833.

[5]. Vaughan L, Giovanello K. Executive function in daily life: Age-related influences of executive processes on instrumental activities of daily living. Psychol Aging 2010. doi:10.1037/a0017729.

[6]. Mograbi DC, Faria C de A, Fichman HC, Paradela EMP, Lourenço RA. Relationship between activities of daily living and cognitive ability in a sample of older adults with heterogeneous educational level. Ann Indian Acad Neurol 2014;17:71–6. doi:10.4103/0972-2327.128558. [PubMed: 24753664]

[7]. Carmichael O, Mungas D, Beckett L, Harvey D, Tomaszewski Farias S, Reed B, et al. MRI predictors of cognitive change in a diverse and carefully characterized elderly population. Neurobiol Aging 2012;33:83–95.e2. doi:10.1016/j.neurobiolaging.2010.01.021. [PubMed: 20359776]

[8]. Cabeza R, Anderson ND, Locantore JK, McIntosh AR. Aging Gracefully: Compensatory Brain Activity in High-Performing Older Adults. Neuroimage 2002;17:1394–402. doi:10.1006/nimg.2002.1280. [PubMed: 12414279]

[9]. Owen AM, McMillan KM, Laird AR, Bullmore E. N-back working memory paradigm: A meta-analysis of normative functional neuroimaging studies. Hum Brain Mapp 2005;25:46–59. doi:10.1002/hbm.20131. [PubMed: 15846822]

[10]. Gomes-Osman J, Indahlastari A, Fried PJ, Cabral DLF, Rice J, Nissim NR, et al. Non-invasive Brain Stimulation: Probing Intracortical Circuits and Improving Cognition in the Aging Brain. Front Aging Neurosci 2018;10. doi:10.3389/fnagi.2018.00177. [PubMed: 29441011]

[11]. Indahlastari A, Albizu A, Nissim NR, Traeger KR, O'Shea A, Woods AJ. Methods to monitor accurate and consistent electrode placements in conventional transcranial electrical stimulation. Brain Stimul 2019;12:267–74. doi:10.1016/j.brs.2018.10.016. [PubMed: 30420198]

[12]. Albizu A, Indahlastari A, Woods AJ. Non-invasive Brain Stimulation BT - Encyclopedia of Gerontology and Population Aging. In: Gu D, Dupre ME, editors., Cham: Springer International Publishing; 2019, p. 1–8. doi:10.1007/978-3-319-69892-2_682-1.

[13]. Jones KT, Stephens JA, Alam M, Bikson M, Berryhill ME. Longitudinal Neurostimulation in Older Adults Improves Working Memory. PLoS One 2015;10:e0121904. doi:10.1371/journal.pone.0121904. [PubMed: 25849358]

[14]. Woods AJ, Antonenko D, Flöel A, Hampstead BM, Clark D, Knotkova H. Transcranial Direct Current Stimulation in Aging Research. Pract. Guid. to Transcranial Direct Curr. Stimul, Cham: Springer International Publishing; 2019, p. 569–95. doi:10.1007/978-3-319-95948-1_19.

[15]. Indahlastari A, Hardcastle C, Albizu A, Alvarez-Alvarado S, Boutzoukas EM, Evangelista ND, et al. A Systematic Review and Meta-Analysis of Transcranial Direct Current Stimulation to Remediate Age-Related Cognitive Decline in Healthy Older Adults. Neuropsychiatr Dis Treat 2021;Volume 17:971–90. doi:10.2147/NDT.S259499. [PubMed: 33824591]

[16]. Nissim NR, O'Shea A, Indahlastari A, Kraft JN, von Mering O, Aksu S, et al. Effects of Transcranial Direct Current Stimulation Paired With Cognitive Training on Functional Connectivity of the Working Memory Network in Older Adults. Front Aging Neurosci 2019;11. doi:10.3389/fnagi.2019.00340. [PubMed: 30837862]

[17]. Martin DM, Liu R, Alonzo A, Green M, Loo CK. Use of transcranial direct current stimulation (tDCS) to enhance cognitive training: effect of timing of stimulation. Exp Brain Res 2014;232:3345–51. doi:10.1007/s00221-014-4022-x. [PubMed: 24992897]

[18]. Nissim NR, O'Shea A, Indahlastari A, Telles R, Richards L, Porges E, et al. Effects of in-Scanner Bilateral Frontal tDCS on Functional Connectivity of the Working Memory Network in Older Adults. Front Aging Neurosci 2019;11. doi:10.3389/fnagi.2019.00051. [PubMed: 30837862]

[19]. Indahlastari A, Chauhan M, Sadleir RJ. Benchmarking transcranial electrical stimulation finite element models: a comparison study. J Neural Eng 2019;16:026019. doi:10.1088/1741-2552/aafbbd. [PubMed: 30605892]

[20]. Sadleir RJ, Vannorsdall TD, Schretlen DJ, Gordon B. Target optimization in transcranial direct current stimulation. Front Psychiatry 2012. doi:10.3389/fpsyt.2012.00090.

[21]. Opitz A, Paulus W, Will S, Antunes A, Thielscher A. Determinants of the electric field during transcranial direct current stimulation. Neuroimage 2015;109:140–50. doi:10.1016/j.neuroimage.2015.01.033. [PubMed: 25613437]

[22]. Datta A, Truong D, Minhas P, Parra LC, Bikson M. Inter-individual variation during transcranial direct current stimulation and normalization of dose using MRI-derived computational models. Front Psychiatry 2012;3. doi:10.3389/fpsyt.2012.00091.

[23]. Indahlastari A, Albizu A, O'Shea A, Forbes MA, Nissim NR, Kraft JN, et al. Modeling transcranial electrical stimulation in the aging brain. Brain Stimul 2020;13:664–74. doi:10.1016/j.brs.2020.02.007. [PubMed: 32289695]

[24]. Laakso I, Tanaka S, Koyama S, De Santis V, Hirata A. Inter-subject variability in electric fields of motor cortical tDCS. Brain Stimul 2015;8:906–13. doi:10.1016/j.brs.2015.05.002. [PubMed: 26026283]

[25]. Halko MA, Datta A, Plow EB, Scaturro J, Bikson M, Merabet LB. Neuroplastic changes following rehabilitative training correlate with regional electrical field induced with tDCS. Neuroimage 2011. doi:10.1016/j.neuroimage.2011.05.026.

[26]. Jamil A, Batsikadze G, Kuo HI, Meesen RLJ, Dechent P, Paulus W, et al. Current intensity- and polarity-specific online and aftereffects of transcranial direct current stimulation: An fMRI study. Hum Brain Mapp 2020. doi:10.1002/hbm.24901.

[27]. Antonenko D, Thielscher A, Saturnino GB, Aydin S, Ittermann B, Grittner U, et al. Towards precise brain stimulation: Is electric field simulation related to neuromodulation? Brain Stimul 2019;12:1159–68. doi:10.1016/j.brs.2019.03.072. [PubMed: 30930209]

[28]. Maldjian JA, Laurienti PJ, Kraft RA, Burdette JH. An automated method for neuroanatomic and cytoarchitectonic atlas-based interrogation of fMRI data sets. Neuroimage 2003;19:1233–9. [PubMed: 12880848]

[29]. Maldjian JA, Laurienti PJ, Burdette JH. Precentral gyrus discrepancy in electronic versions of the Talairach atlas. Neuroimage 2004;21:450–5. [PubMed: 14741682]

[30]. Huang Y, Datta A, Bikson M, Parra LC. Realistic vOlumetric-Approach to Simulate Transcranial Electric Stimulation -- ROAST -- a fully automated open-source pipeline. J Neural Eng 2019. doi:10.1088/1741-2552/ab208d.

[31]. Thielscher A, Antunes A, Saturnino GB. Field modeling for transcranial magnetic stimulation: A useful tool to understand the physiological effects of TMS? Proc. Annu. Int. Conf. IEEE Eng. Med. Biol. Soc. EMBS, 2015. doi:10.1109/EMBC.2015.7318340.

[32]. McCann H, Pisano G, Beltrachini L. Variation in Reported Human Head Tissue Electrical Conductivity Values. Brain Topogr 2019;32:825–58. doi:10.1007/s10548-019-00710-2. [PubMed: 31054104]

[33]. Akhtari M, Bryant HC, Mamelak AN, Heller L, Shih JJ, Mandelkern M, et al. Conductivities of three-layer human skull. Brain Topogr 2000;13:29–42. doi:10.1023/A:1007882102297. [PubMed: 11073092]

[34]. Wagner T, Fregni F, Fecteau S, Grodzinsky A, Zahn M, Pascual-Leone A. Transcranial direct current stimulation: A computer-based human model study. Neuroimage 2007;35:1113–24. doi:10.1016/j.neuroimage.2007.01.027. [PubMed: 17337213]

[35]. Ashburner J SPM: A history. Neuroimage 2012. doi:10.1016/j.neuroimage.2011.10.025.

[36]. Gilad O, Horesh L, Holder DS. Design of electrodes and current limits for low frequency electrical impedance tomography of the brain. Med Biol Eng Comput 2007. doi:10.1007/s11517-007-0209-7.

[37]. Jenkinson M, Beckmann CF, Behrens TEJ, Woolrich MW, Smith SM. FSL. Neuroimage 2012;62:782–90. doi:10.1016/j.neuroimage.2011.09.015. [PubMed: 21979382]

[38]. IBM Corp. Released. IBM SPSS Statistics version 25.0. 2017 2017.

[39]. Ruscio J A probability-based measure of effect size: Robustness to base rates and other factors. Psychol Methods 2008;13:19–30. doi:10.1037/1082-989X.13.1.19. [PubMed: 18331151]

[40]. Truong DQ, Magerowski G, Blackburn GL, Bikson M, Alonso-Alonso M. Computational modeling of transcranial direct current stimulation (tDCS) in obesity: Impact of head fat and dose guidelines. NeuroImage Clin 2013;2:759–66. doi:10.1016/j.nicl.2013.05.011. [PubMed: 24159560]

[41]. Nielsen JD, Madsen KH, Puonti O, Siebner HR, Bauer C, Madsen CG, et al. Automatic skull segmentation from MR images for realistic volume conductor models of the head: Assessment of the state-of-the-art. Neuroimage 2018;174:587–98. doi:10.1016/j.neuroimage.2018.03.001. [PubMed: 29518567]

[42]. Kloss FR, Gassner R. Bone and aging: Effects on the maxillofacial skeleton. Exp Gerontol 2006. doi:10.1016/j.exger.2005.11.005.

[43]. Sun W, Wang H, Zhang J, Yan T, Pei G. Multi-layer skull modeling and importance for tDCS simulation. Proc. 2021 Int. Conf. Bioinforma. Intell. Comput, New York, NY, USA: ACM; 2021, p. 250–6. doi:10.1145/3448748.3448788.

[44]. Opitz A, Paulus W, Will S, Antunes A, Thielscher A. Determinants of the electric field during transcranial direct current stimulation. Neuroimage 2015;109:140–50. doi:10.1016/j.neuroimage.2015.01.033. [PubMed: 25613437]

[45]. Woods AJ, Bryant V, Sacchetti D, Gervits F, Hamilton R. Effects of electrode drift in transcranial direct current stimulation. Brain Stimul 2015. doi:10.1016/j.brs.2014.12.007.

[46]. D'Esposito M, Postle BR, Ballard D, Lease J. Maintenance versus Manipulation of Information Held in Working Memory: An Event-Related fMRI Study. Brain Cogn 1999;41:66–86. doi:10.1006/brcg.1999.1096. [PubMed: 10536086]

[47]. Blumenfeld RS, Nomura EM, Gratton C, D'Esposito M. Lateral prefrontal cortex is organized into parallel dorsal and ventral streams along the rostro-caudal axis. Cereb Cortex 2013;23:2457–66. doi:10.1093/cercor/bhs223. [PubMed: 22879354]

[48]. Goldman-Rakic PS. Regional and cellular fractionation of working memory. Proc Natl Acad Sci U S A 1996;93:13473–80. doi:10.1073/pnas.93.24.13473. [PubMed: 8942959]

[49]. Goldman-Rakic PS. Circuitry of Primate Prefrontal Cortex and Regulation of Behavior by Representational Memory - Comprehensive Physiology. Handb Physiol 1987:373–417.

[50]. Evangelista ND, O'Shea A, Kraft JN, Hausman HK, Boutzoukas EM, Nissim NR, et al. Independent Contributions of Dorsolateral Prefrontal Structure and Function to Working Memory in Healthy Older Adults. Cereb Cortex 2020;00:1–12. doi:10.1093/cercor/bhaa322.

[51]. Trumbo MC, Matzen LE, Coffman BA, Hunter MA, Jones AP, Robinson CSH, et al. Enhanced working memory performance via transcranial direct current stimulation: The possibility of near and far transfer. Neuropsychologia 2016. doi:10.1016/j.neuropsychologia.2016.10.011.

[52]. Nord CL, Lally N, Charpentier CJ. Harnessing electric potential: DLPFC tDCS induces widespread brain perfusion changes. Front Syst Neurosci 2013;7. doi:10.3389/fnsys.2013.00099. [PubMed: 23596400]

[53]. Albizu A, Fang R, Indahlastari A, O'Shea A, Stolte SE, See KB, et al. Machine learning and individual variability in electric field characteristics predict tDCS treatment response. Brain Stimul 2020;13:1753–64. doi:10.1016/j.brs.2020.10.001. [PubMed: 33049412]

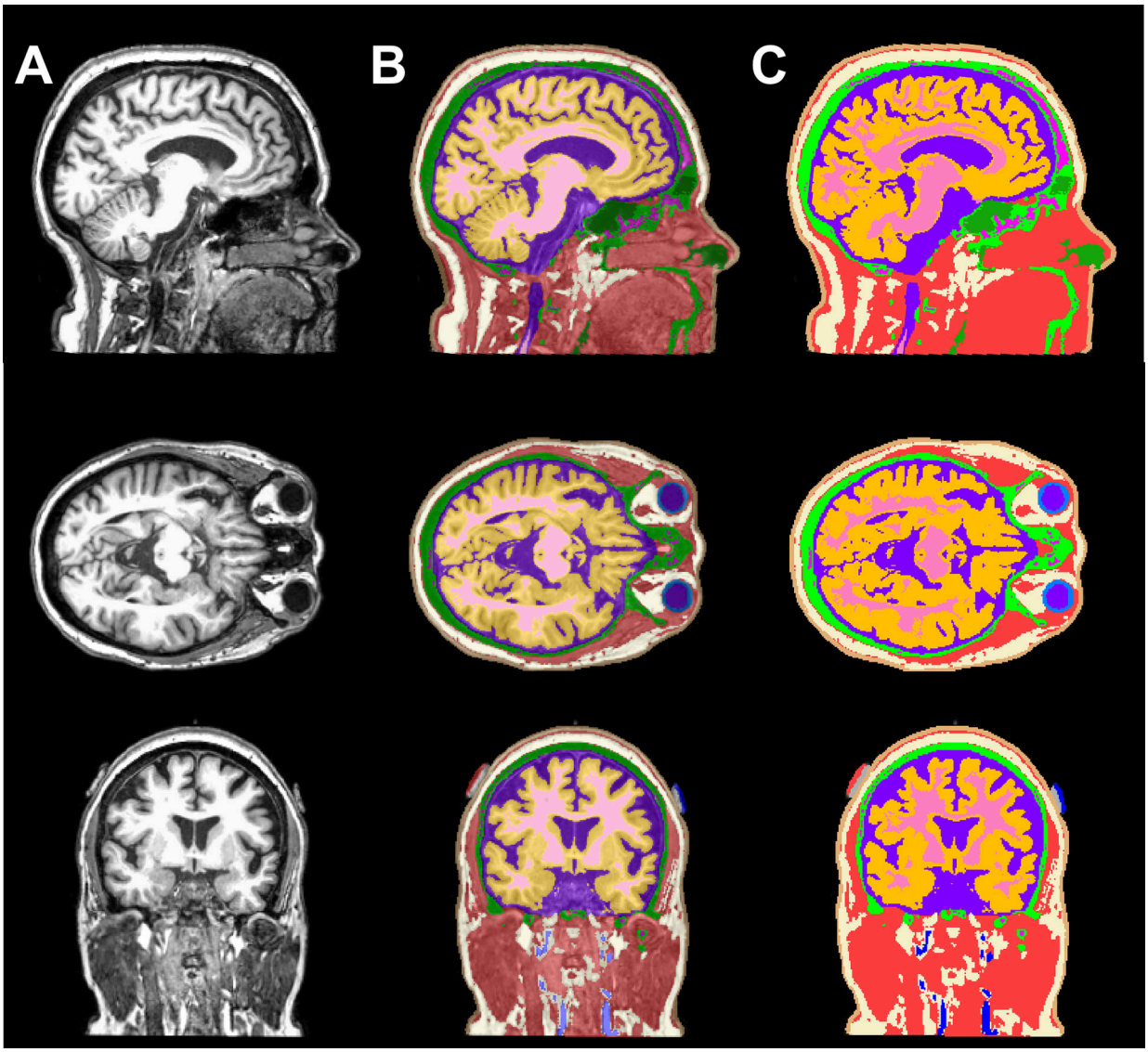

Figure 1.

T1-weighted images and an overlay of T1 images and segmented tissue volumes. A panel view of sagittal, axial, and coronal slice illustrating the A) T1-weighted image, B) 50% translucent overlay and C) 100% opaque overlay to demonstrate the tissue segmentation quality consists of eleven tissue types: white matter (pink), gray matter (orange), CSF (purple), sclera and lens (light blue), blood vessels (dark blue), fat (ivory), muscle (red), skin (brown), air/sinuses (dark green), cancellous (magenta) and cortical bone (light green), as well as the electrode paste (grey) and pads at F3-F4 location (blue and red, respectively).

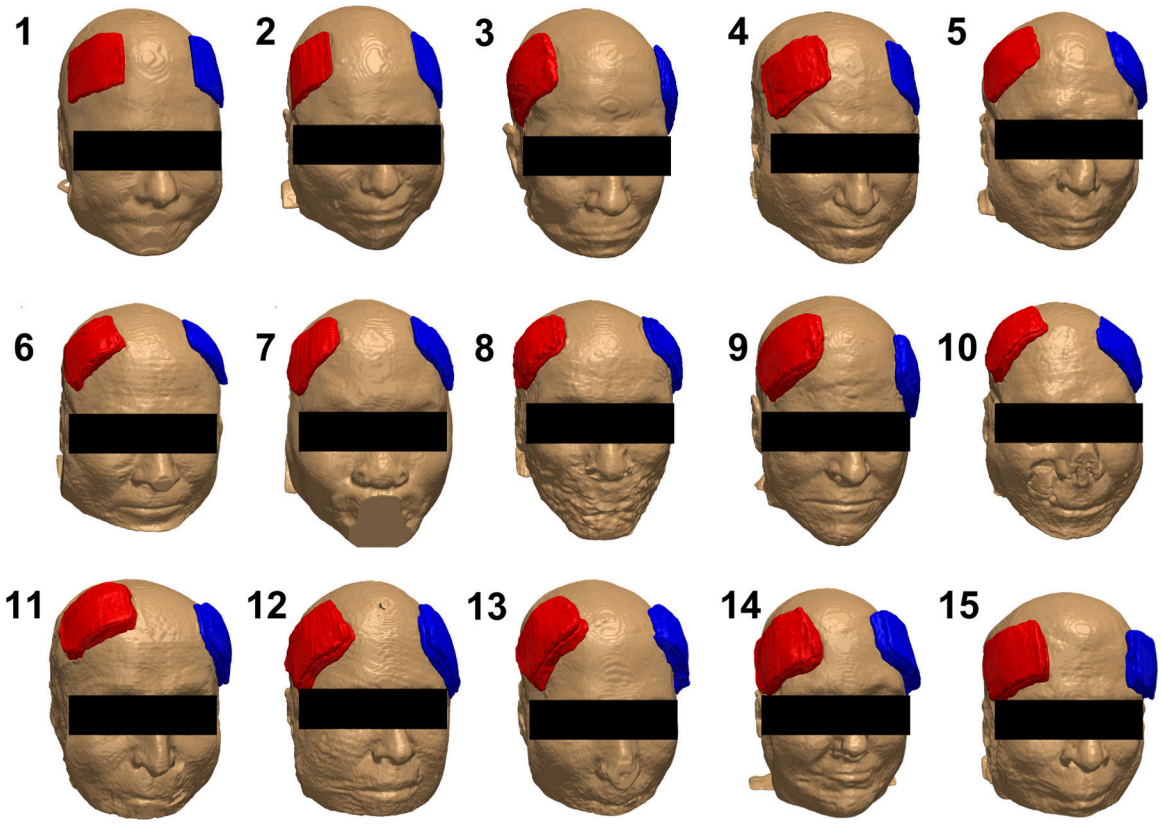

Figure 2.

Electrode placement in fifteen participants. Each electrode (illustrated as a combination of pad and paste) at the anode (red, F4) and cathode (blue, F3) location was manually segmented from captured electrodes in individual T1-weighted images. The participant number is annotated on the top left of each head model.

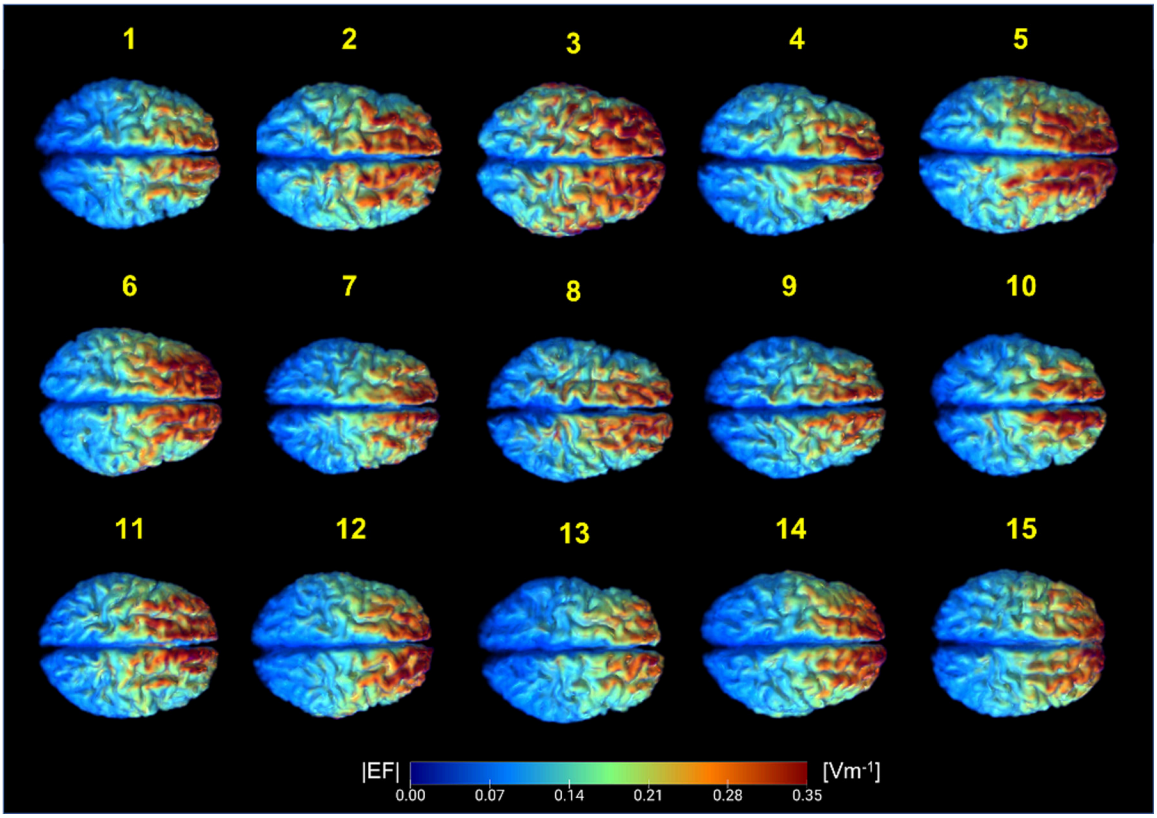

Figure 3.

Generated electric field magnitudes (EF[A/m]) in fifteen head models. Top view of electric field distribution in the brain (white and gray matter) shows non-identical patterns of current delivery across individuals. Each participant is denoted by the yellow numbers on top of each field map.

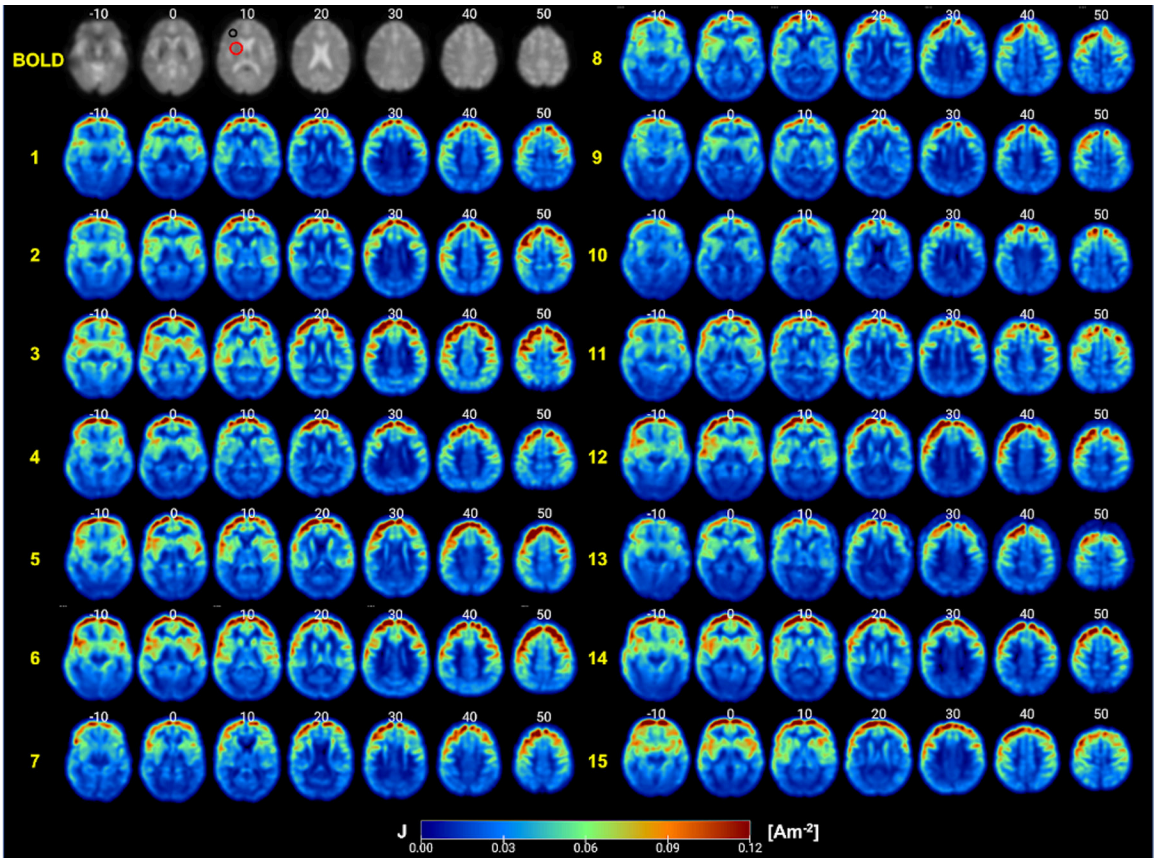

Figure 4.

Generated current density (J[A/m^2]) maps processed according to CONN denoising steps. Axial view representing current density distribution in fifteen participants. Each participant is denoted by the yellow numbers on the left side of each set of image slices. Slice location is denoted by the white numbers on top of each image slice. The left DLPFC regions of interest and the left VLPFC regions of interest are annotated by the black and red circles, respectively. An illustration of a single processed BOLD image is included in top left corner for comparison.

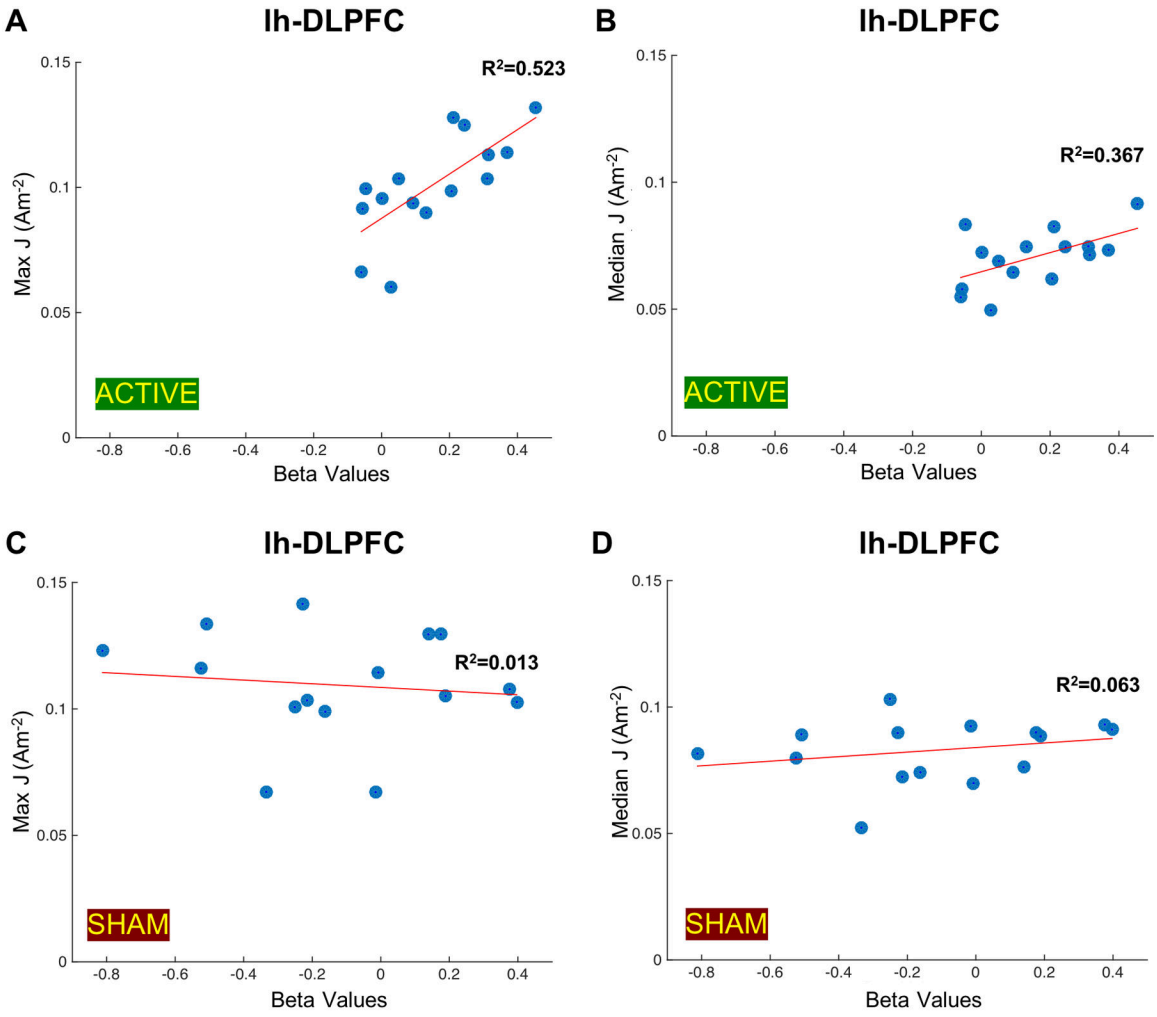

Figure 5.

Correlation plots between generated current densities (J [A/m^2]) in the left DLPFC (lh-DLPFC) ROIs and measured beta values. Measured beta values during active stimulation indicative of the functional connectivity changes between lh-DLPFC and the left VLPFC (lh-VLPFC) ROIs are plotted against A) the maximum current density values in lh-DLPFC ROIs (R^2=0.523, p=0.0023) and B) the median current density values in lh-DLPFC ROIs (R^2=0.0.367, p=0.0168) computed in fifteen participants. Measured beta values during sham stimulation indicative of the functional connectivity changes between lh-DLPFC and lh-VLPFC ROIs are plotted against C) the maximum current density values in lh-DLPFC ROIs (R^2=0.013, p=0.6805) and D) the median current density values in lh-DLPFC ROIs (R^2=0.063, p=0.8772) computed in fifteen participants.

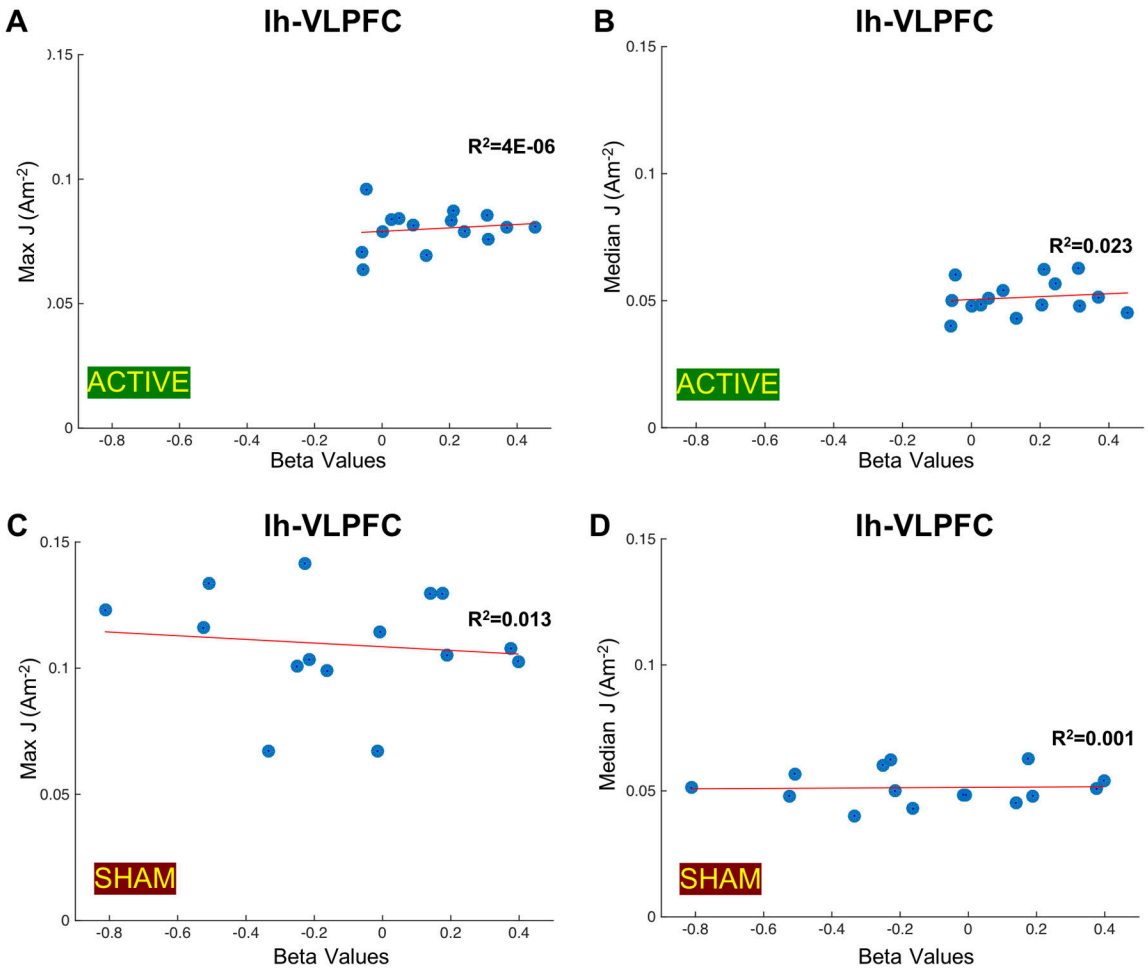

Figure 6.

Correlation plots between generated current densities (J) in the left VLPFC (lh-VLPFC) ROI and measured beta values. Measured beta values during active stimulation indicative of functional connectivity changes between the left DLPFC (lh-DLPFC) and lh-VLPFC ROIs are plotted against A) the maximum current density values in lh-VLPFC ROIs (R^2=4e-06, p=0.6019) and B) the median current density values in lh-VLPFC ROIs (R^2=0.023, p=0.6205) computed in fifteen participants. Measured beta values during sham stimulation indicative of functional connectivity changes between lh-DLPFC and lh-VLPFC ROIs are plotted against C) the maximum current density values in the lh-VLPFC ROIs (R^2=0.013, p=0.4494) and D) the median current density values in the lh-VLPFC ROIs (R^2=0.001, p=0.9029) computed in fifteen participants.